

Summary of doctoral thesis

Title: *Optimization of Additive Manufacturing processes for Fractal geometries production*

Student: Marco Viccica 289139

Supervisors: Flaviana Calignano, Manuela Galati

1 Introduction

The advent of advanced technologies, such as Additive Manufacturing (AM), has pushed designers and manufacturers to develop increasingly efficient and lightweight structures. The ability to manufacture free-shape components permits the exploration of complex features and obtaining tailored structures with enhanced mechanical properties, including energy absorption (EA) characteristics. The theme of energy absorption is strictly correlated to the protection of road users against the numerous accidents that happen every year among different kinds of vehicles. The graph in Fig.1 illustrates the trends of crash fatalities among the most used vehicles during the decade before the COVID-19 pandemic in the European Union (EU) [1].

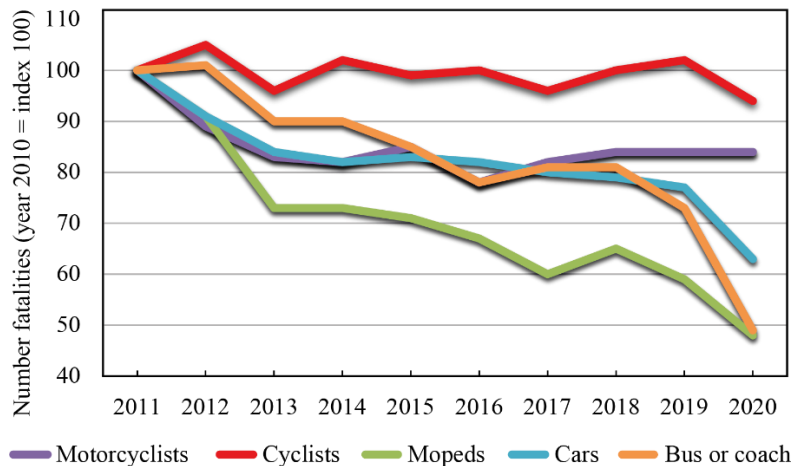


Fig. 1. Trend of fatalities in crashes in the European Union over the period 2010 - 2019 (CARE and Eurostat database [1]).

Together with pedestrians and cyclists, motorcyclists and moped riders form part of the group of “vulnerable road users”. Indeed, 47% of all road fatalities in the EU in 2019 were two-wheel riders. Plus, the “Cyclists” curve has remained constant during the last few years, increasing the worries about the safety of road users who want to embrace green transportation alternatives such as bicycles. Of course, the traffic volumes dropped sharply during the pandemic, which explains the significant drop in road traffic crashes and fatalities. Nevertheless, right after the pandemic

emergency and thanks to the growth of sharing services, micro-mobility has sharply spread around the roads. However, this advent has led to an increase in vulnerable road users and related accidents. Therefore, in recent years, increasing attention has been paid to personal protective equipment (PPE) for impact applications. The energy absorption properties of helmet padding elements in sports, transportation and military fields have been insightfully investigated to develop more efficient and light devices employing complex structures [2–7]. The Fractal geometry is a perfect example of these complex structures.

Fractals are a family of objects whose structure presents the same main shape at all scales of magnification, generating an irregular and chaotic geometric pattern. Besides, a fractal geometry results from subsequent transformations of a simple geometric shape defined as “initiator” [8]. Due to the several process constraints of traditional manufacturing processes, the production of such complex structures can be guaranteed, to date, only by AM technology.

Some studies show how fractal-inspired hierarchical features can result in significant stiffening effects when appropriately designed for AM production. However, there are no studies that investigate the potentiality of a fractal structure produced by AM for energy absorption performance.

The present doctoral thesis aims to characterise the mechanical properties of a fractal structure properly designed for its application in the personal protective equipment field. The production of the developed fractal structure was optimised to be manufactured via a powder bed fusion system for polymers. The energy absorption performances of the structure under different designs were investigated with a huge number of compression tests at low and high strain rates. A material comparison was performed to analyse the mechanical performance of the structure when produced with two polymers characterised by highly different stiffness.

2 Materials and methods

The developed fractal structure was inspired by the mathematical 3D Greek cross presented by the mathematician Dickau R. [9]. The initiator consists of a cross of three struts linearly extruded along the axes of a cartesian tern (Fig. 2a). Each strut has a circular cross-section of diameter D that is constant at each step and an initial strut length L . At each following iteration, two more branches extruded along the remaining axes are added to the half strut by obtaining six Greek cross fractal structures scaled of one half. The iteration steps used to generate the 3D cross-based fractal structure (3D-CFS) are highlighted, with different colours, in Fig. 2a.

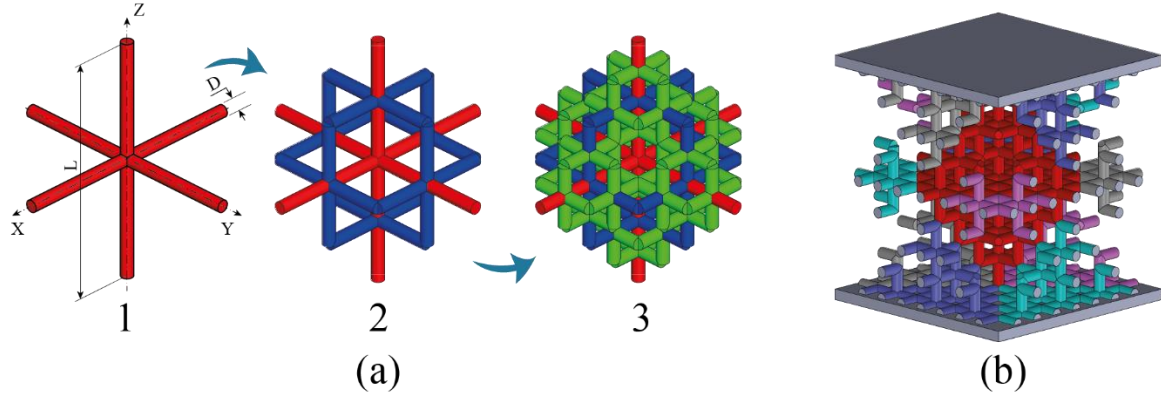


Fig. 2. a) 3D-CFS iterations: in red, the first step; in blue and green, the added branches of the second and third step, respectively; (b) cubic compression sample. (adapted from Ref. [10]).

The 3D-CFS design is parametric, and its global size depends on the two critical parameters mentioned above, L and D . To evaluate the mechanical properties of the fractal structure, a cubic compressive test sample was developed by applying proper transformations starting from the third iteration of the 3D-CFS. The first configuration proposed for the preliminary experimental tests consisted of a 3D-CFS developed in a cubic envelope of 40 mm side and 2 mm long diameter struts.

The samples were manufactured with the Formiga Velocis P110 (EOS GmbH) and recycled PA2200 powder (EOS tradename of the polyamide 12 or PA12) to simulate industrial conditions. This AM process is based on the polymeric powder bed fusion system with a laser source (PBF-L/P). Since the powder bed is subjected to preheating phases, it remains warm and compact enough to surround the fused sections of the part without the use of support structures. This building strategy makes the PBF-L/P the better polymeric AM solution for producing such intricate reticular structures. Each configuration was manufactured in five replicas for statistical purposes.

After the production, quasi-static compression tests were performed using a universal testing machine, 3MZ Easydur, equipped with a load cell of 5 tonnes. The crosshead speed for the compression tests was set to 5 mm/min, corresponding to a quasi-static (QS) strain rate.

The porosity and dimensional accuracy of the printed specimens were analysed by computed tomography scanning (CT-scan) (GE Phoenix v|tome|x s).

As the first characterisation of the developed structure, a production optimisation was performed by focusing on the production constraints of the selected process. Due to the well-known influence of the build orientation on the mechanical properties of additively manufactured parts, the

construction orientation variation of the structure was investigated. The selected orientations are shown in Fig. 3. Each orientation sample was tested under the same load condition of compression.

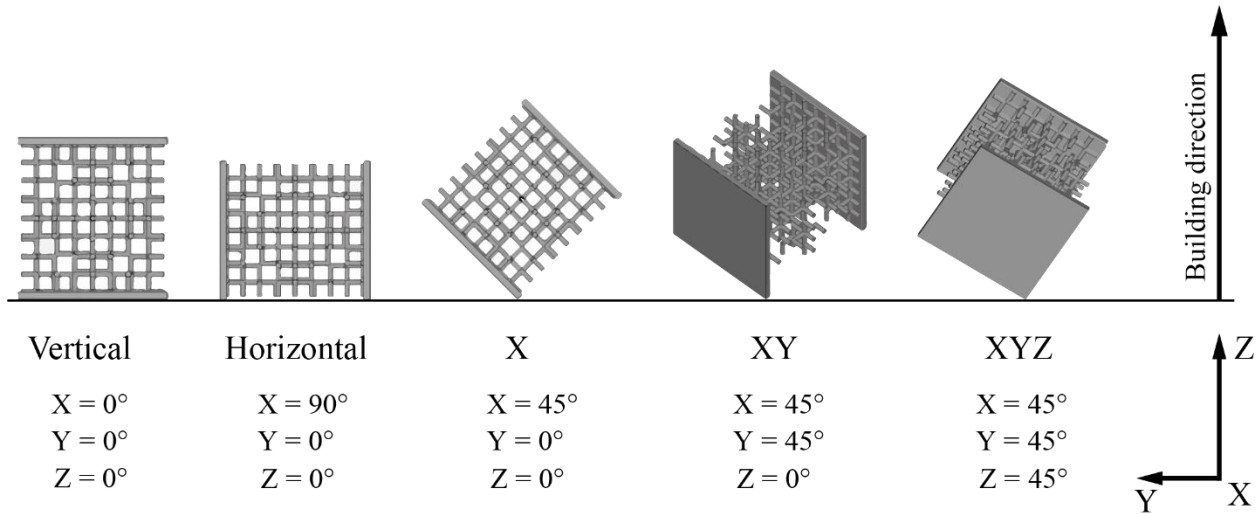


Fig. 3. Five configurations of 3D-CFS build orientation according to standard angles rotation around the three axes of the reference system.

The effect on the strut diameter variation was investigated to evaluate the limit of the selected manufacturing process in producing thin features. Four configurations of the 3D-CFS were designed by varying the strut diameter from 2.5 mm to 1 mm, as shown in Fig. 4.

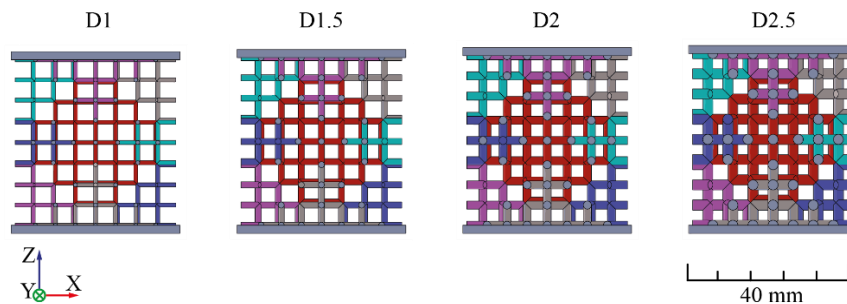


Fig. 4. Diameter variation of the 3D-CFS: from left to right, the diameter size varied from 1 mm to 2.5 mm.

The diameter variation implies the geometric density alteration of the structure. The geometric density, also known as volume fraction (VF), represents the ratio between the actual volume of the reticular structure and its cubic envelope.

Once produced, the investigated samples were tested under compression test to evaluate the variation of the mechanical characteristics with the D parameter.

A successive step of production optimisation was conducted by designing a feasibility study to evaluate the manufacturability of the 3D-CFS with different geometric densities. Thus, a full

factorial plan was designed considering two geometrical factors, L and D, which are characterised by six levels each. In detail, the strut length varied from 20 to 40 mm, whereas the strut diameter from 1.6 mm to 2.6 mm. The designed plan consisted of 36 combinations of 3D-CFS structures with a volume fraction variation from 6.1% to 39%.

Each design is named using a combination of L and D variables followed by the identification of their own level, for instance, L20_D1.6. The VF value increases with the length decrease and decreases with the reduction of the strut diameter, as illustrated graphically in Fig. 5.

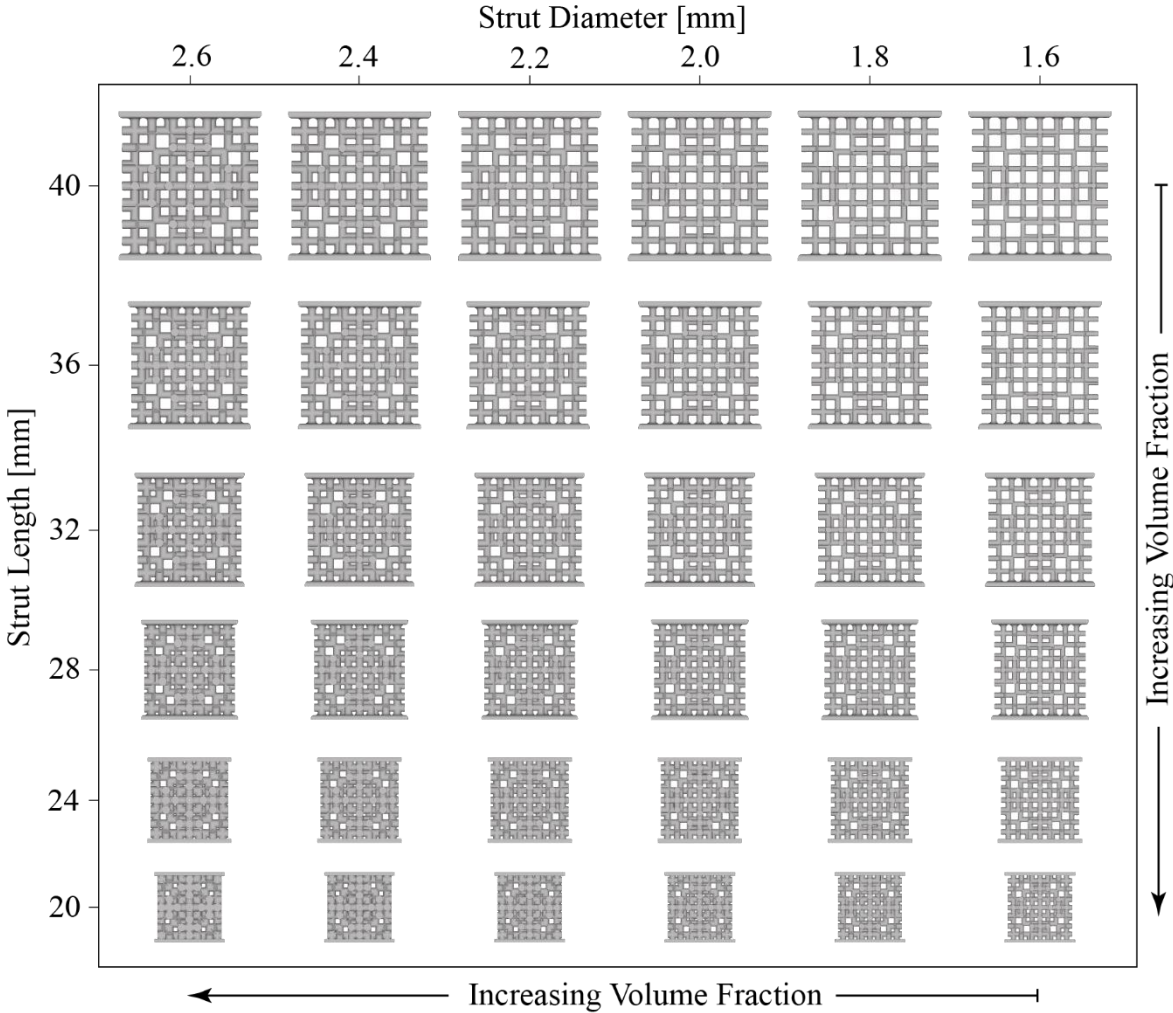


Fig. 5. CAD illustration of the full factorial design plan based on the variation of the volume fraction factor.

The designs that provided optimal results regarding manufacturability were then selected and analysed to evaluate their mechanical properties and energy absorption performances.

The evaluation of the energy absorption (EA) properties was conducted by computing the specific energy absorption (SEA) parameter, which takes into account the material density (ρ) of the tested component (Eq.1).

$$SEA = \frac{W}{\rho} \quad (1)$$

Where W is the energy per unit volume (W) (Eq. 2), i.e., the area under the stress (σ) vs strain (ε) curve until the strain point in which starts the densification phase (ε_d).

$$W = \int_0^{\varepsilon_d} \sigma(\varepsilon) d\varepsilon \quad (2)$$

Although evaluating the absorbed energy could be satisfactory to estimate the absorption capabilities of the examined structure, further descriptors can help design a device with optimal absorber performance characterised by a maximum transmitted stress combined with a long deformation. Thus, the total Ideality (I_t) efficiency parameter was computed as indicated in Eq. 3.

$$I_t = \frac{\int_0^{\varepsilon_i} \sigma(\varepsilon) d\varepsilon}{\max_{0 \leq \varepsilon \leq \varepsilon_i} \sigma \cdot \varepsilon_i} \quad (3)$$

The I_t parameter curve against the strain permits to identify the onset densification. Indeed, the absorber structure reaches its maximum efficiency value right before the densification phase in the compressive diagram, in which the structure collapses without significant energy absorption. The onset densification determination is graphically reported in Fig. 6.

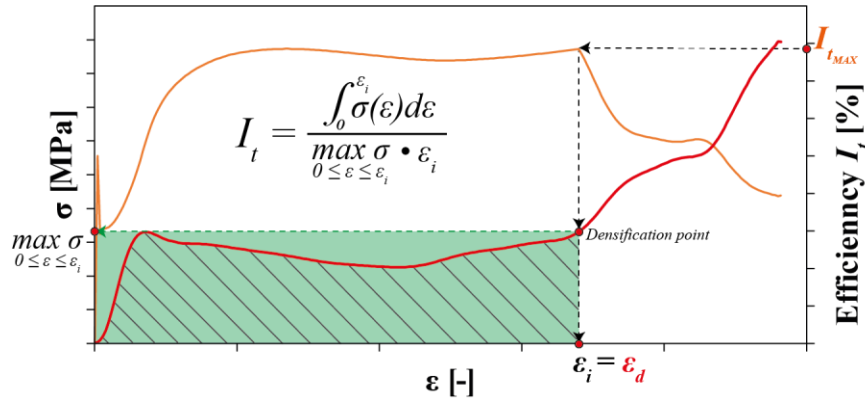


Fig. 6. Localisation of the densification point of the stress-strain curve (red line) at the maximum value of the efficiency parameter I_t (orange line). The filled area under the red line represents the absorbed energy per unit volume until the ε_d ; the green area is the reference energy of an ideal absorber.

Since the ideal absorber should keep the instant peak force below a prescribed threshold with almost constant stress for a long deformation strictly proportional to the energy impact [11], the

analysed structure should exhibit a good stiffness and elongation balance. Consequently, a further material was selected for the investigation of the EA properties of the 3D-CFS.

The second material employed in this research work was the thermoplastic polyurethane (TPU) processed with a similar AM process with which the PA12 samples were produced. Thus, five 3D-CFS configurations extracted from the full factorial design plan shown in Fig. 5. were selected for the material comparison between the PA12 and TPU polymers. The five configurations are characterised by different volume fraction, as reported in Fig. 7.

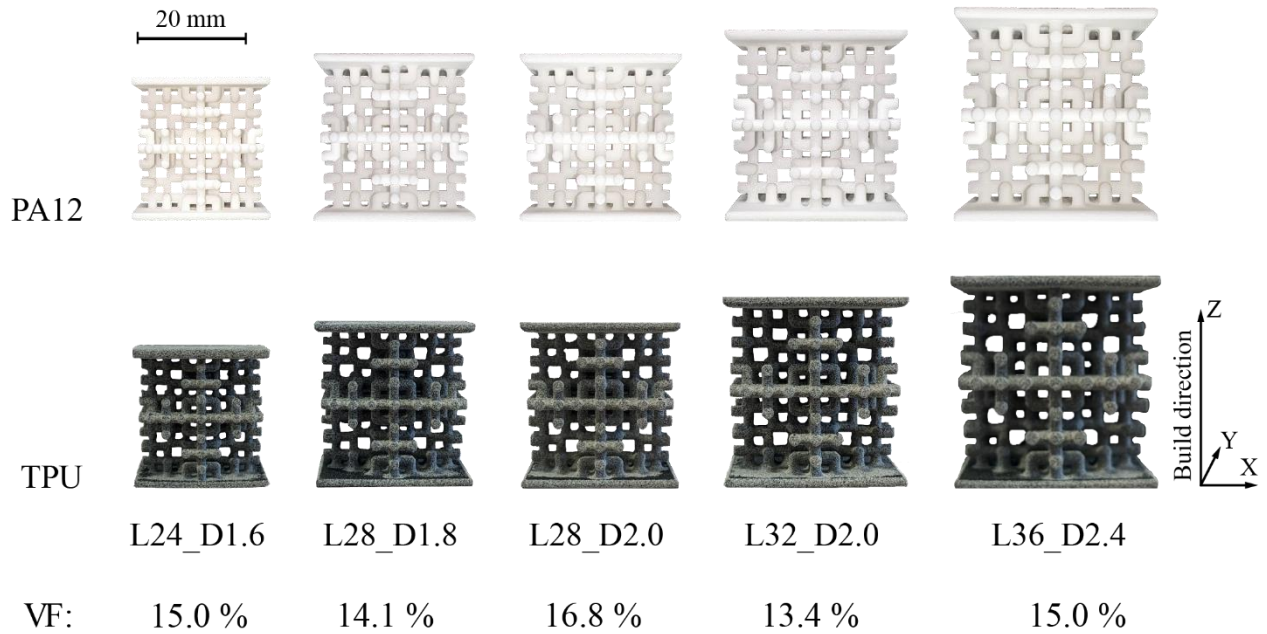


Fig. 7. PA12 and TPU printed samples with multiple configurations extracted by the full factorial design plan.

Three replicas of each configuration were produced and tested with high-speed (HS) compression loads. A drop tower machine was used to test the 3D-CFS specimens at HS impact with an initial kinetic energy of 25J.

In addition, the strain rate dependency of the PA12 material was investigated by comparing the mechanical properties of the above nominated configurations tested in QS and HS compression loads.

A further index of the capability to absorb energy is related to the actual force recorded during the impact. Thus, the acceleration, evaluated in g (gravitational acceleration constant), was calculated from the force vector. When the acceleration is plotted against the time, it is common to consider the maximum value of the curve, i.e., the peak acceleration (PA), as an indicator of the damage

quantity that the protected object can tolerate. Specific PPE applications typically require this value below a certain threshold [12].

Finally, a finite element model was developed to analyse and predict the deformation mechanisms and the mechanical behaviour of the structure under low strain rate compression loads. Thus, the material model of the polyamide 12 processed via PBF-L/P was modelled by implementing the bulk material results obtained experimentally. Once calibrated the mechanical properties of the PA12 numerical model, the 3D-CFS geometry was discretised with a tetrahedral element mesh, and the load conditions of a quasi-static compression test were set on the structure. The numerical results of the simulated compression test were compared to the experimental counterparts to validate the FE model.

3 Results

The results of mechanical behaviour under compression test at low strain rate of the five L40_D2.0 configurations with different orientations are reported in the stress vs strain graph of Fig. 8. The horizontal configuration shows the highest strength response. However, the other configurations show similar results to the horizontal one, except for the vertical orientation, which presents a significantly lower compression curve. These results are strictly related to the orientation of the vertical and horizontal struts of the structure. Indeed, since the additive manufacturing process is based on a layer-by-layer strategy, the orientation of the part is a crucial parameter. Therefore, vertical-oriented struts present numerous little sections compared to horizontal ones, which are manufactured with fewer and wider sections. When the load is applied along the longitudinal axis of the strut, a better strength for the horizontal-oriented strut is observed.

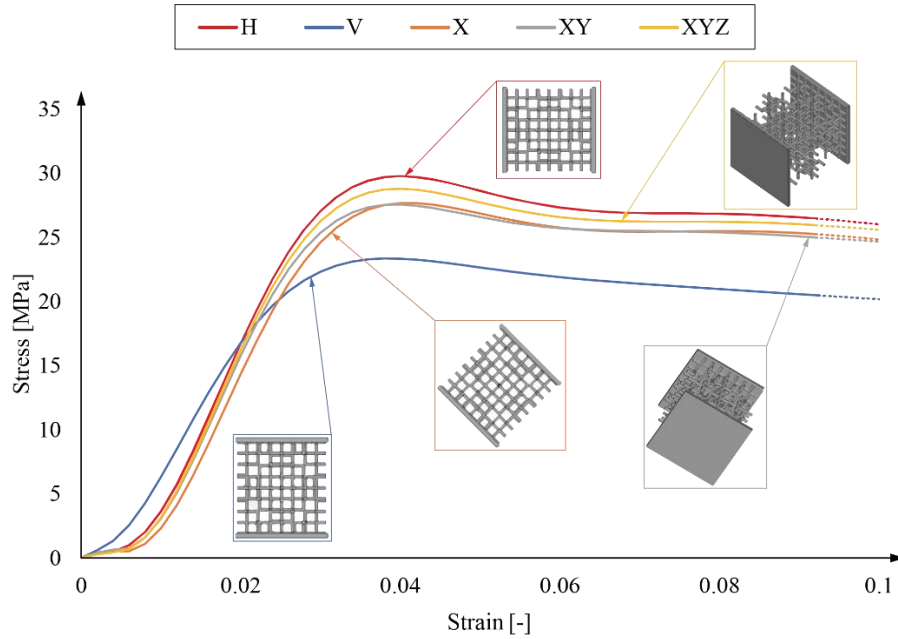


Fig. 8. Stress vs strain graph of the 3D-CFS structure manufactured with five different build orientations.

These results are strictly related to the orientation of the vertical and horizontal struts of the structure. Indeed, since the additive manufacturing process is based on a layer-by-layer strategy, the orientation of the part is a crucial parameter. Therefore, vertical-oriented struts present numerous little sections compared to horizontal ones, which are manufactured with fewer and wider sections. When the load is applied along the longitudinal axis of the strut, a better strength for the horizontal-oriented strut is observed. Since the axial force applied to the vertically oriented configuration is loaded mainly on the vertical-oriented struts, the compression strength of the structure shows the worst results. Consequently, this orientation was conservatively selected for the following experiments to evaluate the fractal performances in its worst manufactured scenario.

The variation of the strut diameter was analysed by maintaining the cubic envelope of 40 mm and the third fractal iteration. The experimental results of the compression test on the fractal structures with different strut diameters are shown in Fig. 9. The variation of the strut diameter linearly reduces the structure stiffness. However, by comparing the first peak of the curves, there is a higher decrease in the strength of the 1 mm diameter 3D-CFS structure.

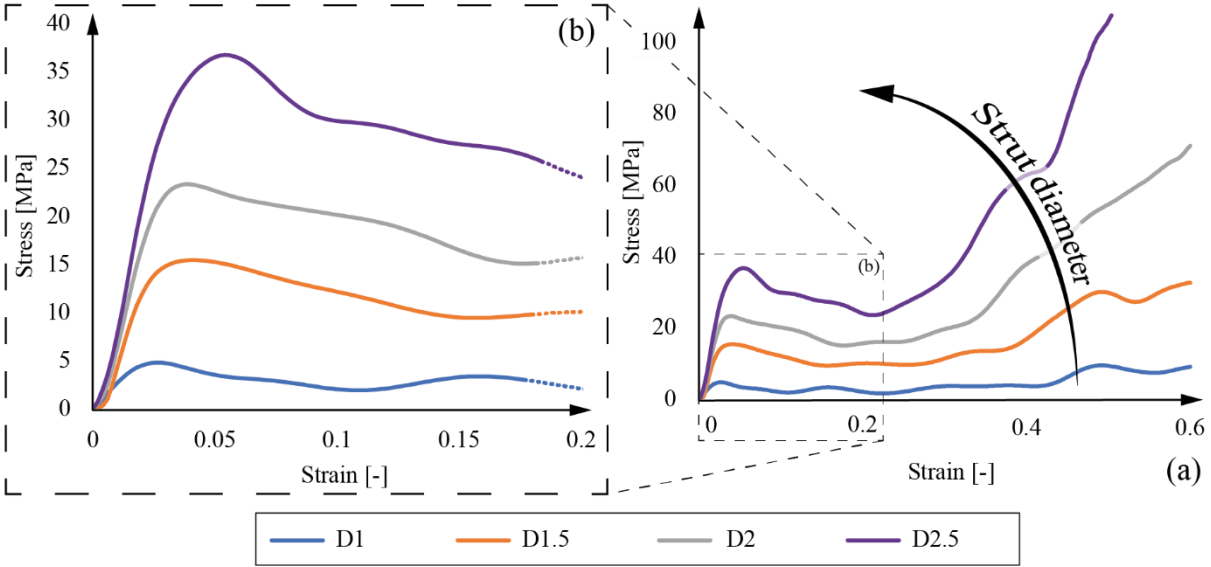


Fig. 9. (a) Experimental stress-strain curve of 3D-CFS specimens with a different strut diameter; (b) detailed graph in the 0-20% strain range.

These results may be explained by considering a more remarkable effect of the process-induced defects (porosities and shape of the strut) on the mechanical performance of the structure. As an example, Fig. 10 compares sections of D1 and D2 specimens obtained by CT scan analysis. The presence of multiple internal porosities can be detected in both D1 and D2 struts. Even if in fewer numbers, the porosities in the thinner structure appear to be less circular and bigger. The printed struts along and perpendicular to the build direction show an average diameter size of 0.93 ± 0.25 mm and 1.88 ± 0.23 mm for the D1 and D2 specimens, respectively, which is comparable with the nominal counterparts. However, the horizontal struts of the D1 specimen present a significant shape deviation from the nominal circular cross-section (Fig. 10b).

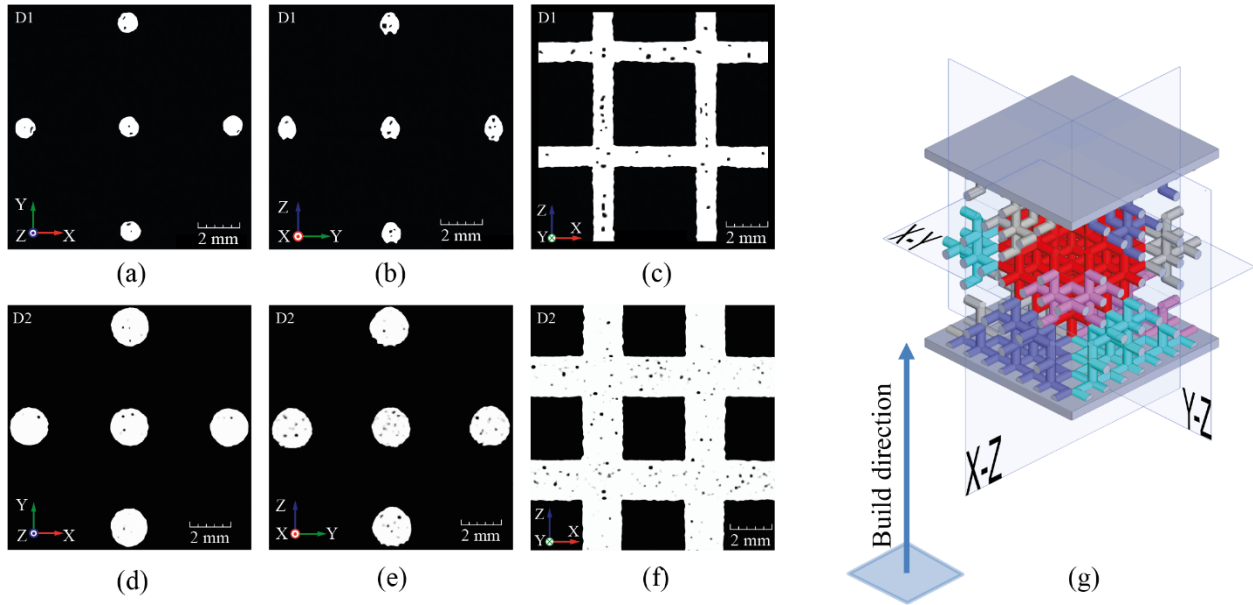


Fig. 10. CT-scan images of D1 (top) and D2 (bottom) specimens in different cross-sections. The pores are visible in black. (a)-(d) Y-X plane-section of the vertical struts; (b)-(e) Z-Y plane-section of the horizontal struts; (c)-(f) Z-Y plane-section at the middle position of the struts.

These findings were applied when designing an explorative study about the manufacturability and mechanical characteristics of the developed structure. The experimental plane included different configurations of the structure obtained by varying the length and diameter of the strut. Fig. 11 illustrates all the manufactured and cleaned samples in which the colours indicate the amount of removed powder, where red represents a part in which residual powder is still present and green a structure completely free. The obtained results reveal that configurations with the higher capability of being fully powder-free are characterised by values of the nominal minimum gap of internal pores higher than around 1.40 mm, which corresponds to 3D-CFS with VF higher than 15%.

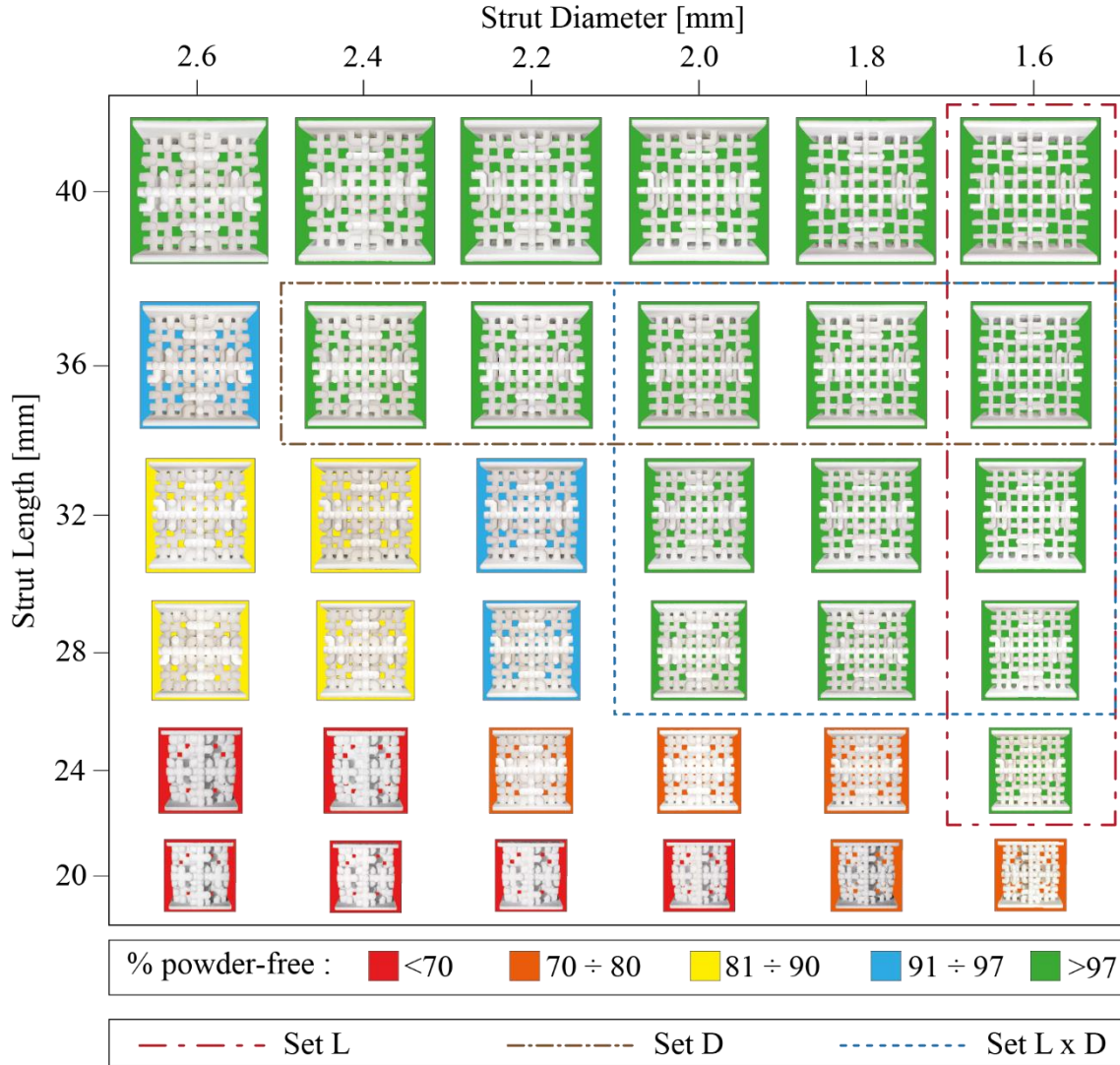


Fig. 11. Map of the powder-free percentage evaluated for the set of 36 3D-CFS configurations manufactured via PBF-L/P in PA12 material. Coloured areas represent the percentage of powder-free: red (<70%), orange (70 ÷ 80%), yellow (81 ÷ 90%), light blue (91 ÷ 97%), green (>97%). Dotted lines with different patterns enclose the configurations selected for the analysis of mini set, respectively, Set L, Set D, Set LxD.

According to the results mentioned above, the analysis of the mechanical performance investigation was restricted to three different sets of 3D-CFS structures extracted from the one characterised by a higher percentage of powder-free, namely “Set L”, “Set D”, and “Set LxD”.

The quasi-static compression test results of the three sets are depicted in Fig. 12. The results show that when the L parameter decreases with constant D , higher strength values are obtained. Conversely, the increase of the diameter with constant length increases the strength. Overall, all these results are strictly related to the VF variation of the fractal geometry that corresponds to a quasi-linear variation of the structure strength and decrease of the plateau region.

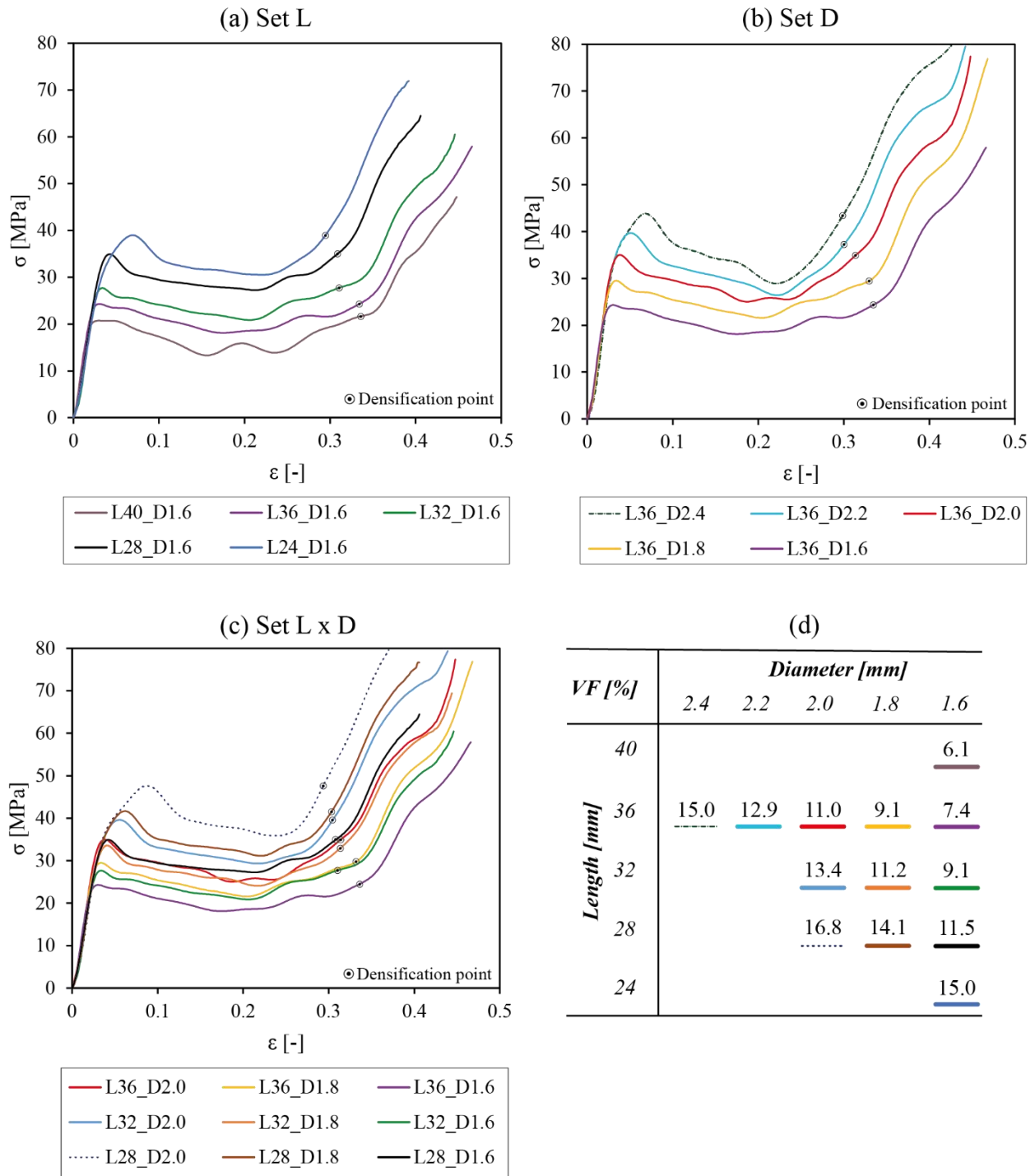


Fig. 12. Stress vs strain curves of the compression test in quasi-static strain rate performed on PA12 samples with configurations belonging to (a) Set L, (b) Set D, and (c) Set LxD. (d) Resume table of volume fraction values of the tested structures.

It is worth noting that, even if the levels of strength vary with the VF, the QS compressive curves of the tested structures highlight similar deformation behaviour. These similarities are explained

by the low deformation rate that guarantees a more controlled bending behaviour of the struts, leading to easier movement replication among different configurations. Therefore, a material strain rate dependency study was performed to investigate the behaviour of the structure when test under different strain rate compression loads. Fig. 13 reports the comparison between the selected five configurations tested in QS and HS. The tests at high strain rate impact loads on PA12 samples showed a significant discrepancy in terms of deformation mechanisms of the structure compared to the same configurations tested in quasi-static (QS) compression load. The high-speed movement of the impactor mass reduces that capability to compress and close the internal porosities of the struts with the axis parallel to the load direction exhibited in the low deformation regime. Therefore, the compression strength of the structure is reduced in the first part of the curve, which corresponds to a decrease in Young's modulus compared to the QS samples. Moreover, except for the L36_D2.4 configuration, the plateau region shows an ascending behaviour that can be caused by a reduction of bending deformation among the struts combined with more rapid internal structure collapse.

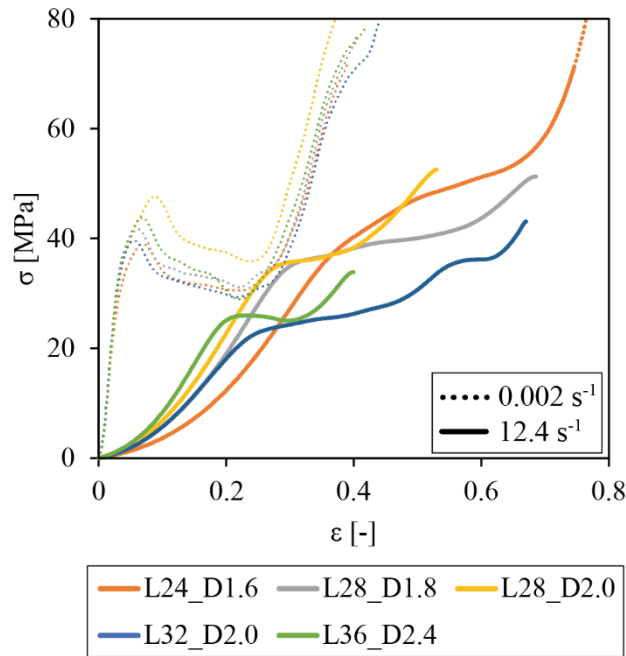


Fig. 13. Stress-strain curves of five PA12 3D-CFS configurations tested under low (0.002 s^{-1}) and high (12.4 s^{-1}) strain rate compression loads.

Further HS impact tests were made to investigate the differences between the PA12 and TPU materials in absorbing energy during impact events. The results of the comparison are shown in Fig.14. The stress vs strain curves highlight the substantial difference in stiffness and strength of

the two investigated materials. PA12 samples reached stress values almost double those of the TPU counterparts. However, analysing the tested samples revealed a moderate elastic recovery of the TPU structures with a very low quantity of fractures around the struts' nodes compared to the PA12 counterparts. The low stiffness of the TPU material guaranteed that the structure accommodated more easily the bending behaviour of vertical and horizontal struts as observed in the same structures analysed at low strain rate compression. These findings are confirmed by the constant stress value on the plateau region reported in most tested samples.

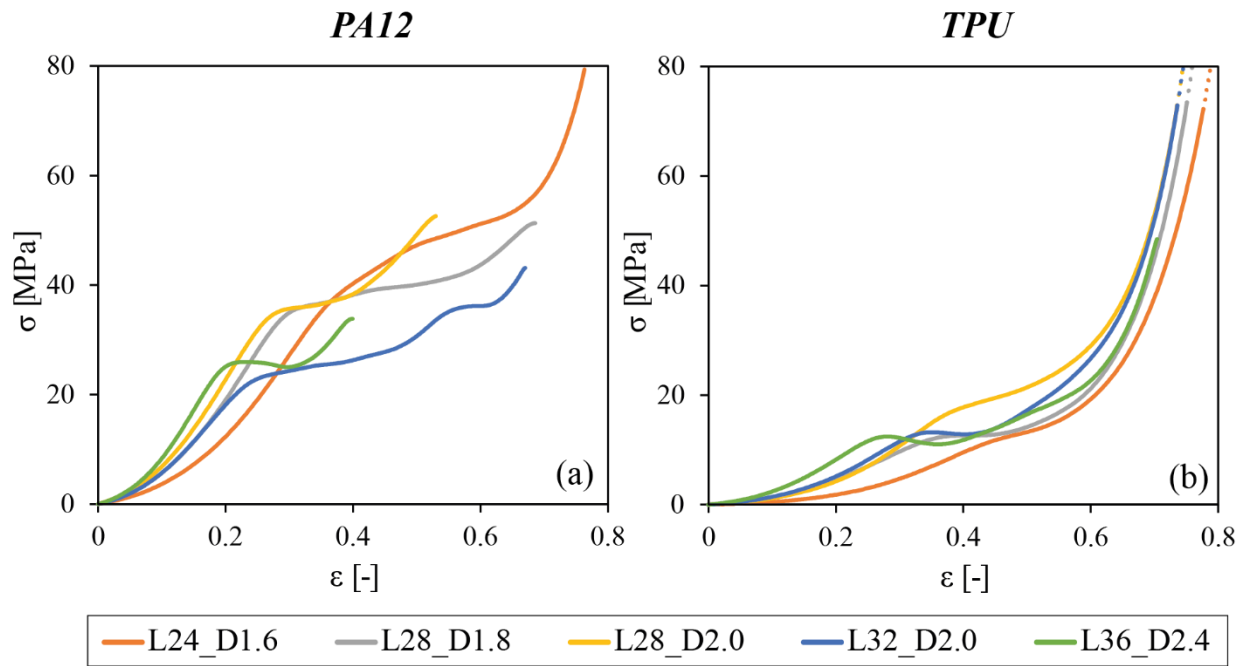


Fig. 14. Stress vs strain graph of high strain rate compression load tests of (a) PA12 and (b) TPU samples.

The differences in strength between the two materials are emphasized by the evaluation of the SEA parameter, which results are graphically illustrated in the bar plot of Fig. 15a. However, as mentioned before, the more controlled deformation mechanisms of TPU structures lead to generating low discrepancies in SEA values among the different configurations.

Even if accentuated flatted stress-strain curves characterise the TPU samples, their lower stiffness generates less EA efficiency than the PA12 configurations (see Fig. 15b).

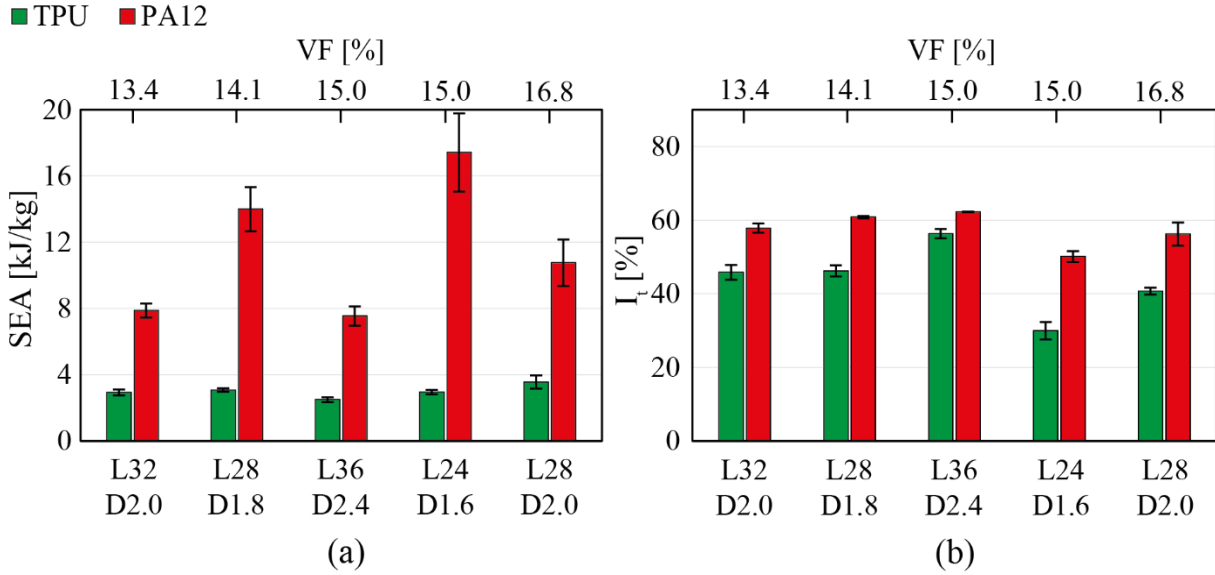


Fig. 15. (a) Specific energy absorption (SEA) and (b) total Ideality (I_t) bar plots of PA12 and TPU 3D-CFS configurations tested with high-speed compression loads. The graphs report the mean value and standard deviation evaluated among the three replicas of each tested configuration.

The acceleration vs time graph is reported in Fig. 16. The comparison between the two materials illustrates that PA12 samples can absorb more energy with lower peak of acceleration (PA) values than the TPU samples. PA12 configurations are characterised by a decrease of the PA with the VF decrease. In contrast, the TPU counterparts show a dependency on the PA with the diameter of the struts. As reported in Fig. 16b, it can be observed the same behaviour between the couples L24_D1.6/L28_D1.8 and L28_D2.0/L32_D2.0.

Optimal PA values are achieved for both materials with the configuration L36_D2.4. This trend is also confirmed by the total Ideality index (Fig. 15b). The higher diameter dimension could explain the superior performance of the L36_D2.4 than the other investigated configurations. Indeed, as observed from the tomography images, the mechanical performances of artefacts produced via the PBF process are affected by the presence of internal pores that increase their damage effect with the decrease of the wall-thickness, or diameter in case of struts.

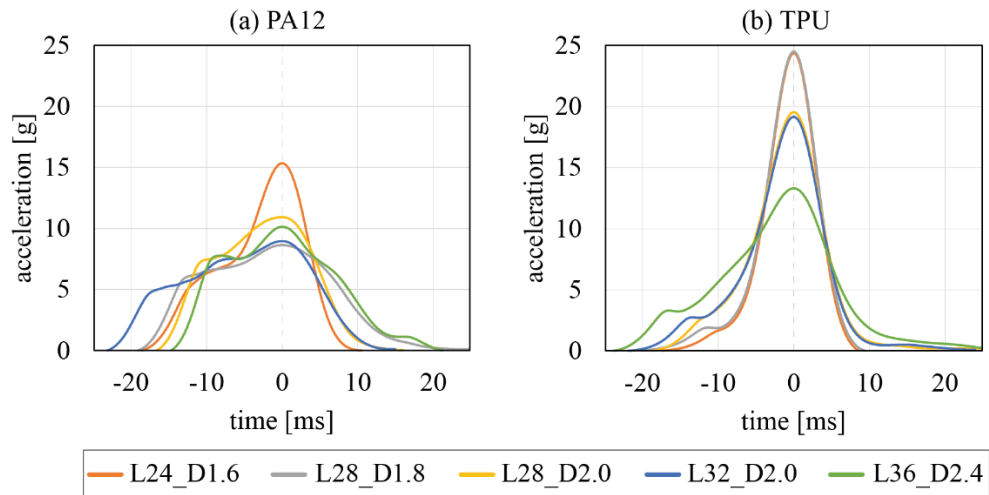


Fig. 16. Acceleration vs time graph of the 3D-CFS samples manufactured in (a) PA12 and (b) TPU materials. Each curve is centered with respect to the main peak of acceleration.

The comparison between the experimental and numerical model of the L40_D2.0 structure is reported in the stress vs strain graph of Fig. 17. As it can be observed, the numerical model emulates well the structure deformation. In terms of stress, the deviation between the experimental and numerical results is constant during the test, indicating a systematic effect that may be neglected in the modelling.

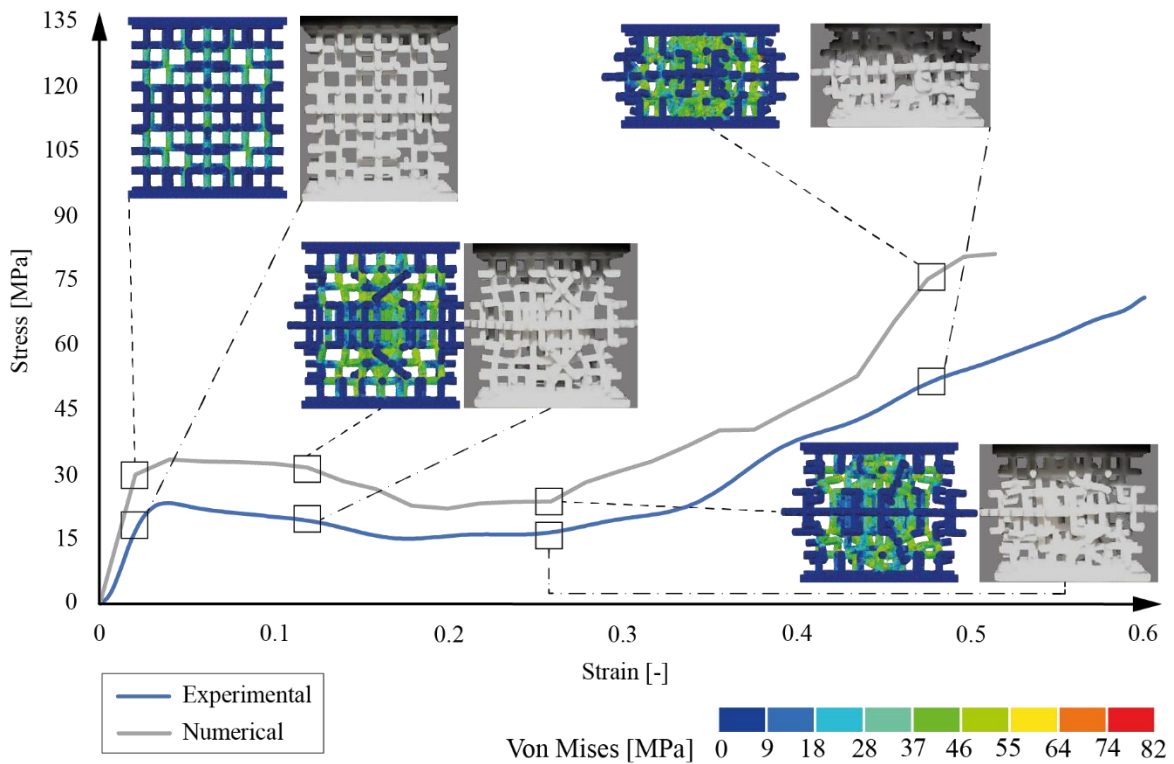


Fig. 17. Comparison between the experimental and numerical results of the D2 with its four different strain levels frame.

The simulation of the compression test shows that the higher stresses are localised in the horizontal and vertical-oriented struts because of the combination of more deformation mechanisms. The external vertical struts bend with a bell-shaped curve along the compression load (highlighted by the dotted red line in Fig. 18). This deformation is combined with a torsion around the Z axis of the central fractal structure with higher rotation degrees at the centre group of struts (Fig. 18). The torsion deformation allows for the creation of a wider plateau region of the stress-strain graph and a more controlled compression. The structure reaches a rotation up to about 45° in the middle before the starting of the densification phase (cross-section A-A in Fig. 18). By considering constant the L value of 3D-CFS, higher values of diameter size increase the stiffness of the structure, because the reduction of the torsion deformation and the increasing of the stress around the nodes leading to premature fractures.

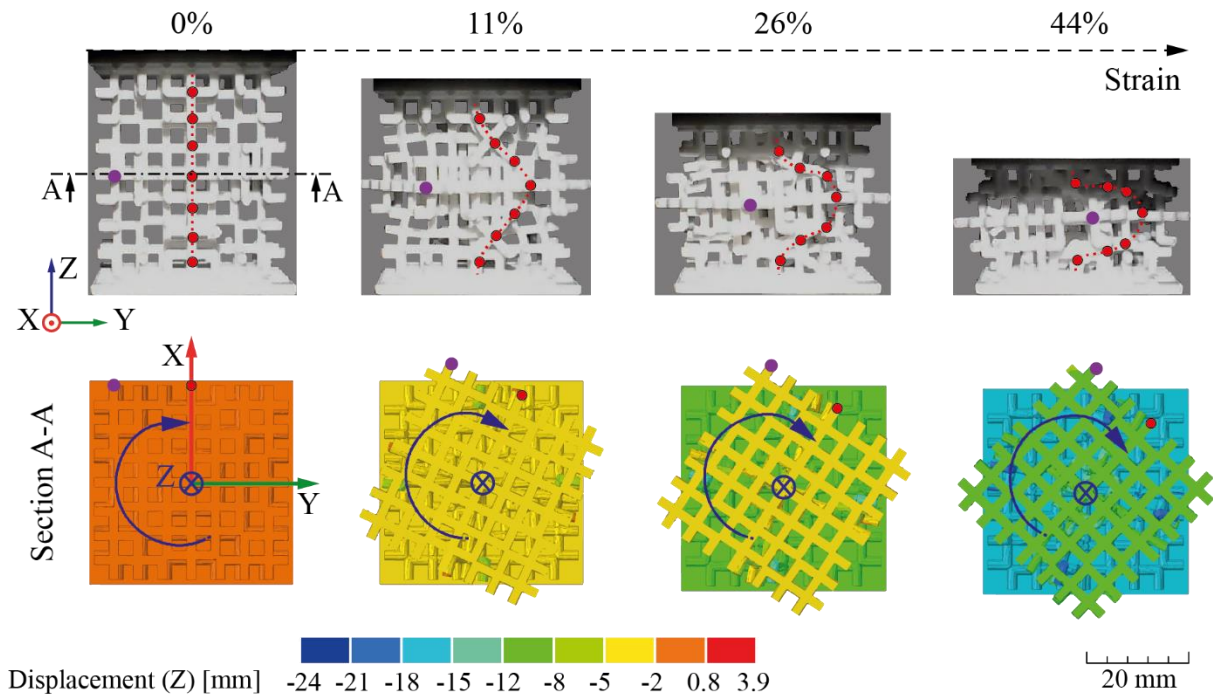


Fig. 18. Deformation mechanisms. In the top, experimental deformation up to 44% of strain for the D2 structure; the dotted red line represents the bending of the external vertical struts, which assumes a bell-shaped curve along the compression. Section A-A reported in the bottom, extrapolated by the FE model, highlights the corresponding torsion deformation of the structure up to 45° of rotation around the Z axis.

Conclusions

The present doctoral thesis work aimed to characterise the energy absorption capabilities of a 3D cross-based fractal structure (3D-CFS) manufactured via an advanced manufacturing technology: additive manufacturing. The fractal structure was designed to be manufactured via the powder bed fusion (PBF) technique by employing two different polymers, polyamide 12 (PA12) and thermoplastic polyurethane (TPU). From a first characterisation of the fractal structure, it was identified the build orientation that best represents an industrial production. Moreover, the diameter variation study showed that features of thickness below 1.5mm accentuated the effect of process-induced defects in decreasing the mechanical properties of the structure.

The main geometrical parameters of the structure, i.e., the length (L) and the diameter (D) of the strut, were varied in several combinations to generate multiple 3D-CFS structures with different volume fractions. The variation of the VF was studied first to individuate the manufacturability limit in producing this kind of complex structure via PBF. These experiments have determined the window of the geometrical parameters, limiting the study to a reduced group of configurations. These structures were then tested under quasi-static compression loads to evaluate the energy absorption performance with the VF variation. The results revealed that the increase of the VF implies an increase in specific energy absorption (SEA) but a decrease in the total Ideality parameter due to the high-stress response. Even if these findings have suggested that low VF 3D-CFS represent the optimal energy absorber under a low strain rate compression load, the impact tests have shown that these structures perform better with an average value of VF. Indeed, the brittle behaviour of the PA12 and the low stiffness of TPU affect the strength of the structure due to the premature struts' collapse. Despite the permanent plastic deformation, the PA12 3D-CFS structures guarantee superior EA performances with lower peak acceleration than TPU counterparts when subjected to 25 J energy level impact. Also, the results of PA12 show higher EA characteristics than other additively manufactured cellular structures and up to 170% of SEA higher than a typical material employed for head PPE, i.e., EPS foam. In contrast, the elasticity and recovery capabilities of the TPU material can be suitable for multiple impact conditions.

A limitation of the present research is represented by the low energy level the developed structure can tolerate. Indeed, the standard tests applied for personal protective equipment require at least 50J of energy impact resistance. Even though the present fractal structure was tested as a single unit cell, real applications require cell replication to cover the desired device area subjected to the

impact. Consequently, further experimental investigations are needed to evaluate the EA capabilities of the 3D-CFS designed in a multiple-cell configuration and tested under higher kinetic energy impact loads.

Dissemination

The presentation of the developed structure and its first characterisation was partially presented at the 16th CIRP conference on Intelligent computation in manufacturing engineering [13] in 2022 and published in a *Procedia CIRP* in 2023. A more detailed paper was published in the *Thin-Walled Structures* journal (6.4 of Impact Factor) [10], reaching up to date four citations.

The following results regarding the impact tests performed in collaboration with the research group of Professor R. de Sousa were presented at the Italian Workshop on Shell and Spatial Structures conference in 2023, which paper will be published soon in the book of proceedings under the *Lecture Notes in Civil Engineering* book series, edited by Springer and indexed in Scopus.

Numerical modelling methods used in this thesis work were also explored to analyse the mechanical behaviour of composite components manufactured with another AM process based on the filament extrusion, and the related results were published in 2021 in the *Polymer Testing* journal [14] (5.1 Impact Factor) reaching up to date nine citations.

Finally, the rules of the Design for Additive Manufacturing employed for the fractal structure design and production were insightful investigated also in the papers published in the *Crystals* journal [15] (2.7 of Impact Factor) and presented at the 31st CIRP Design Conference 2021 [16], reaching up to date eleven and one citations, respectively.

Bibliography

- [1] European Road Safety Observatory, European Road Safety Observatory. Facts and Figures - Motorcyclists and moped riders - 2023, 2023. https://road-safety.transport.ec.europa.eu/statistics-and-analysis/data-and-analysis/facts-and-figures_en.
- [2] Najmon, J.C., J. Dehart, Z. Wood, A. Tovar, Cellular Helmet Liner Design through Bio-inspired Structures and Topology Optimization of Compliant Mechanism Lattices, *SAE Int. J. Transp. Saf.* 6 (2018) 217–235. <https://doi.org/10.4271/2018-01-1057>.
- [3] Jafferson, J.M., S. Pattanashetti, Use of 3D printing in production of personal protective equipment (PPE) - A review, *Mater. Today Proc.* 46 (2021) 1247–1260. <https://doi.org/10.1016/j.matpr.2021.02.072>.
- [4] Khosroshahi, S.F., S.A. Tsampas, U. Galvanetto, Feasibility study on the use of a hierarchical lattice architecture for helmet liners, *Mater. Today Commun.* 14 (2018) 312–323. <https://doi.org/10.1016/j.mtcomm.2018.02.002>.
- [5] Montgomery, S.M., H. Hilborn, C.M. Hamel, X. Kuang, K.N. Long, H.J. Qi, The 3D printing and modeling of functionally graded Kelvin foams for controlling crushing performance, *Extrem. Mech. Lett.* 46 (2021) 101323. <https://doi.org/10.1016/j.eml.2021.101323>.
- [6] Clough, E.C., T.A. Plaisted, Z.C. Eckel, K. Cante, J.M. Hundley, T.A. Schaedler, Elastomeric Microlattice Impact Attenuators, *Matter.* 1 (2019) 1519–1531. <https://doi.org/10.1016/j.matt.2019.10.004>.
- [7] Kim, H., S.H. Tawfick, W.P. King, Buckling elastomeric springs and lattices for tailored energy absorption, *Mater. Today Commun.* 35 (2023) 106417. <https://doi.org/10.1016/j.mtcomm.2023.106417>.
- [8] Peitgen, H.-O., H. Jürgens, D. Saupe, *Chaos and fractals: new frontiers of science*, Springer Science & Business Media, 2006.
- [9] Dickau, R., Greek Cross Fractal, (2008). <https://www.robertdickau.com/greekcross.html> (accessed February 10, 2022).
- [10] Viccica, M., M. Galati, F. Calignano, L. Iuliano, Design, additive manufacturing, and characterisation of a three-dimensional cross-based fractal structure for shock absorption,

- Thin-Walled Struct. 181 (2022) 110106.
<https://doi.org/https://doi.org/10.1016/j.tws.2022.110106>.
- [11] Wierzbicki, T., Energy absorption of structures and materials, 2004.
<https://doi.org/10.1016/j.ijimpeng.2003.12.004>.
- [12] Fernandes, F.A.O., R.J. Alves De Sousa, Motorcycle helmets - A state of the art review, *Accid. Anal. Prev.* 56 (2013) 1–21. <https://doi.org/10.1016/j.aap.2013.03.011>.
- [13] Viccica, M., M. Galati, F. Calignano, L. Iuliano, An additively manufactured fractal structure for impact absorption applications, *Procedia CIRP.* 118 (2023) 793–798.
<https://doi.org/10.1016/j.procir.2023.06.136>.
- [14] Galati, M., M. Viccica, P. Minetola, A finite element approach for the prediction of the mechanical behaviour of layered composites produced by Continuous Filament Fabrication (CFF), *Polym. Test.* 98 (2021) 107181.
<https://doi.org/10.1016/j.polymertesting.2021.107181>.
- [15] Galati, M., F. Calignano, M. Viccica, L. Iuliano, Additive Manufacturing Redesigning of Metallic Parts for High Precision Machines, *Crystals.* 10 (2020) 161.
- [16] Ercolini, E., F. Calignano, M. Galati, M. Viccica, L. Iuliano, Redesigning a flexural joint for metal-based additive manufacturing, *Procedia CIRP.* 100 (2021) 469–475.
<https://doi.org/10.1016/j.procir.2021.05.106>.